Extended Defects in CdZnTe Radiation Detectors

Aleksey E. Bolotnikov, *Member, IEEE*, Stephen O. Babalola, Giuseppe S. Camarda, Henry Chen, *Member, IEEE*, S. Awadalla, Yonggang Cui, *Member, IEEE*, Stephrn U. Egarievwe, Petro M. Fochuk, Rastgo Hawrami, Anwar Hossain, Jesse R. James, I. J. Nakonechnyj, J. Mackenzie, Ge Yang, Chao Xu, and Ralph B. James, *Fellow, IEEE*

***Abstract*—Large-volume CdZnTe (CZT) single crystals with electron lifetime exceeding 10 μs have recently become commercially available. This opened the opportunity for making room temperature CZT gamma-ray detectors with extended thicknesses and larger effective areas. However, the extended defects that are present even in the highest-quality material remain a major drawback which affects the availability and cost of large CZT detectors. In contrast to the point defects that control electron lifetime and whose effects on the charge collection can be electronically corrected, the extended defects introduce significant fluctuations in the collected charge, which increase with a crystal's thickness. The extended defects limit the uniformity in the electrons' drift distance in CZT crystals, above which electron trapping cannot effectively be corrected. In this paper, we illustrate the roles of the extended defects in CZT detectors with different geometries. We emphasize that the crystallinity of commercial CZT materials remains a major obstacle on the path to developing thick, large-volume CZT detectors for gamma-ray imaging and spectroscopy.**

***Index Terms*—CdZnTe, crystal defects, radiation detectors.**

I. Introduction

LARGE-VOLUME single crystal CdZnTe (CZT) with electron lifetimes exceeding 10 μs have recently become available. This opened an opportunity for making CZT devices with extended thicknesses and effective areas for detection and imaging of gamma rays [1], [2] in the energy range up to several MeV. Despite these improvements in crystal growth techniques, today, the large-volume CZT detectors are still very rare. This signifies that other defects, which are present even in the highest-quality material, remain a major drawback which reduces availability and increases cost of large-volume CZT detectors. So far, the largest CZT detectors reported in the literature are 6-cm^3 pixel devices developed by the University of Michigan [3]; their total number is counted by tens.

The goal of this work is to emphasize that today's commercial spectroscopy grade CZT material has excessively high concentrations of extended defects that limit the performance and production yield of large-volume CZT detectors, and whose importance was less significant in thin devices.

Several types of extended defects can be identified in a typical commercial detector-grade CZT crystal: twins, sub-grain boundaries, Te inclusions, and dislocations which are often arranged in, so-called, dislocation walls. Most of these defects are not readily seen with the naked eye, or under an IR microscope, so that crystal screening and selection is a time consuming and difficult task.

The transmission IR microscope can reveal inclusions down to ~ 1 μm. Twins and grain boundaries crossing a crystal can be identified on the lapped surface by observing the contrast pattern in the reflection light images. This approach, however, does not work in the cases of dislocations and low-angle boundaries. Special techniques, such as surface etching, diffraction topography and transmission electron microscopy, are required for their identification. Some of these techniques are destructive and are not always available to vendors. Only when twin boundaries and grown-in-type dislocations are decorated by secondary phases can they be identified with IR microscopy.

It is well known that the extended defects can impair the performance of semiconductor devices. Their specific effects were thoroughly studied in many semiconductors, especially Si and Ge (see, e.g., [4]). In the latter case, the research, driven by semiconductor industry, helped to develop new techniques for crystal growth that eventually resulted in a stable supply of relatively defect-free wafers.

A cumulative effect of the extended defects increases with the device's thicknesses and can be seen as a reduction in the overall device's performance. The roles of the particular defects can be identified by correlating their signatures with the non-uniformities in the device's response.

In this work, we studied commercial CZT detectors by using the material characterization techniques available at Brookhaven National Laboratory (BNL).

II. Experimental

We employed three experimental techniques to identify the extended defects in CZT material: transmission IR microscopy,

Manuscript received November 26, 2008; revised December 29, 2008 and February 11, 2009. Current version published August 12, 2009. This work was supported by U.S. Department of Energy, Office of Nonproliferation Research and Development, NA-22 and Defense Threat Reduction Agency. The manuscript has been authored by Brookhaven Science Associates, LLC under Contract No. DE-AC02-98CH1-886 with the U.S. Department of Energy.

A. E. Bolotnikov, G. S. Camarda, Y. Cui, A. Hossain, G. Yang, C. Xu, and R. B. James are with Brookhaven National Laboratory, Upton, NY 11793 USA (e-mail: bolotnik@bnl.gov; camarda@bnl.gov; cui@bnl.gov; hossain@bnl.gov; gyang@bnl.gov; mgcclx@gmail.com; rjames@bnl.gov).

S. O. Babalola is with Fisk University, Nashville, TN 37208 USA and Vanderbilt University, Nashville, TN 37235, USA (e-mail: balabola@bnl.gov).

H. Chen, S. Awadalla, and J. Mackenzie are with Redlen Technologies, Sidney, Canada (e-mail: henry.chen@redlen.com; awagalla@redlen.com; mackenzie@redlen.com).

S. U. Egarievwe is with Vanderbilt University, Nashville, TN 37235 USA (e-mail: segariev@bnl.gov).

P. M. Fochuk and I. J. Nakonechnyj are with Chernivtsi National University, Chernivtsi, 58012, Ukraine (e-mail: fochukp@gmail.com; Nakonechnyj@bnl.gov).

R. Hawrami is with Fisk University, Nashville, TN 37208 USA (e-mail: hawrami@bnl.gov).

J. R. James is with Tennessee Technological University, Cookeville, TN 38505 USA (e-mail: sixshooter21@gmail.com).

Digital Object Identifier 10.1109/TNS.2009.2019960

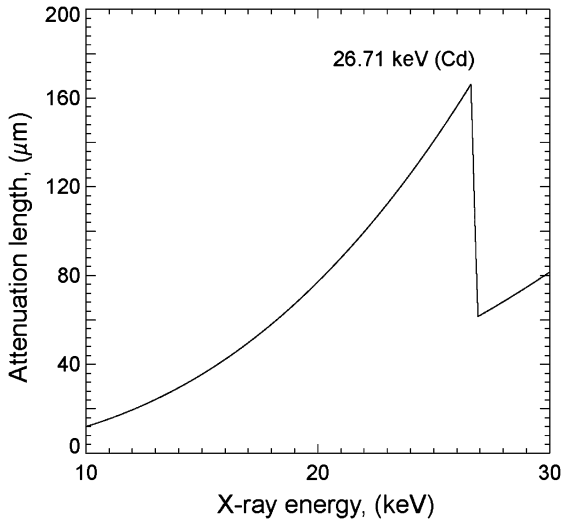

Fig. 1. X-ray attenuation length in CZT material.

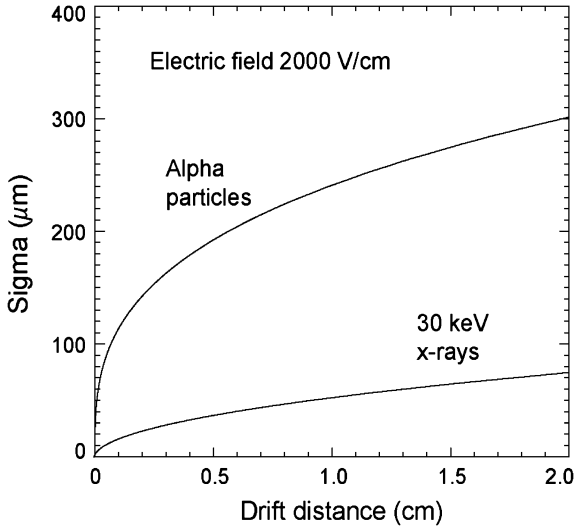

Fig. 2. Calculated spread (sigma) of the electron cloud generated by 5.5 MeV alpha-particles, and 30 keV X-rays versus drift distance.

white X-ray beam diffraction topography, and surface etching with a Nakagawa solution. These techniques, widely used for material characterizations, were described elsewhere [5]–[7].

We use transmitted X-rays to generate the diffraction topography contrasts imaged with a photosensitive paper. The contrasts in the topography images allow us to identify crystal's diffracting planes and presence of the large extended defects, e.g., subgrain boundaries and dislocation walls associated with crystal's strains. The interested reader is referred to Authier's book [8] for a complete description of the technique.

The high-resolution X-ray mapping system, which utilized a synchrotron radiation beam, is our primary tool for measuring the non-uniformities in the charge losses caused by the crystal defects. The spatial resolution of the measured response maps is limited by the diffusion of the electron (or hole) cloud generated by the low-energy X-rays, for which electrostatic repulsion can be neglected [9]. By varying the photon energies from 15 to 30 keV, we can control the X-ray penetration depth and so distinguish surface- and bulk-effects (Fig. 1).

The X-ray response maps can be generated by collecting either electrons or holes, provided that the latter have the sufficiently high $\mu\tau$-product and can generate signals with amplitudes above the noise threshold. We term them electron (e-) and hole (h-) collection maps, correspondingly. By collecting the holes at a high bias applied across a device, we significantly increase the sensitivity of the mapping system to the charge-trapping defects and, at the same time, preserve high spatial-resolution. Indeed, the diffusion process is independent of a carriers' type. The width (sigma) of the charge cloud is given by

$$\sigma = \sqrt{2Dt} = \sqrt{\frac{4kTL}{eE}} \tag{1}$$

where kT/e is the thermal energy measured in eV, E is the electric-field's strength, and L is the drift distance. In contrast, the amount of charge loss due to trapping depends on the carriers' drift velocity, $V_{\rm drift}$:

$$Q_{col} = Q_0 e^{-\frac{L}{V_{\rm drift}\tau}}. \tag{2}$$

For holes, the drift velocity is $\sim$10 times smaller than that of electrons. We note that due to strong electrostatic repulsion, the width of the electron clouds generated by alpha particles, when the latter are used for testing a device's response, is about an order-of-magnitude wider than the width of the cloud generated by low energy X-rays (see Fig. 2) [9]. Consequently, alpha particles are sensitive to only the very large Te inclusions ($\sim$ 20-μm diameter or larger).

Although most measurements we report here were taken with spectroscopy grade Redlen crystals, our findings are equally applicable to the samples we receive from other vendors and institutions. Other supplier's material suffers the similar problems.

III. Results and Discussion

A. Twins and Sub-Grain Boundaries

Extensive studies have explored the effects of twins and low-angle (sub-grain) boundaries on charge transport in CZT crystals (see, e.g., [4]). The boundaries can be considered as walls of edge dislocations that affect the transport of charge carriers in several ways [10]–[13]. Dangling bonds, existing within dislocation cores, accumulate space charge. Accordingly, the boundary planes form potential barriers for drifting carriers. Electrical conduction along dislocation cores also may affect the local electric field. Enhanced diffusion within twin and sub-grain boundaries causes the dislocations to accumulate secondary phases that are opaque to carriers. Finally, charged dislocations may attract impurities that increase charge trapping along the boundaries. We note that all these effects strongly depend on the boundaries' orientations with respect to the direction of electron drift.

Fig. 3 shows IR photographs of the etched CZT samples containing twins taken under mixed lighting, transmission and reflection, to reveal the texture of the surface and the inclusion-decorated boundaries in the bulk. Etching clearly revealed the locations of the twin boundaries exiting the crystal surfaces. One can also see the Te inclusions decorating the dislocations within the boundaries. The inclusions precisely follow the

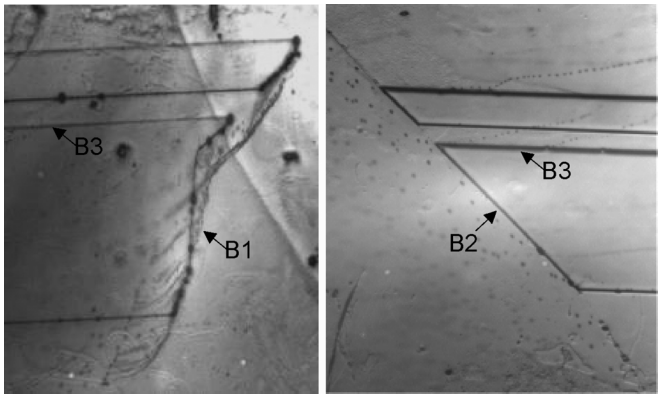

Fig. 3. IR photographs of the etched CZT samples containing twins taken under reflection and transmission light. Te inclusions, seen in transmission IR light, help to localize the twin boundaries in the bulk: twin terminating (B1) and lateral (B2) with high densities of dislocations. The dislocation-free the first order twin boundary (B3) contains no secondary phases.

shape of the twin terminating boundary (B1) and the lateral twin boundaries (B2) that have high density of dislocations. In contrast, no inclusions are visible within the dislocations-free boundary (B3) which is probably the {111}-{111} first order twin boundary. Since Te inclusions tend to decorate dislocations, IR transmission microscopy reveals both the dislocations within twin boundaries and individual linear dislocations formed during the crystal's growth. We note that dislocations arranged in the walls or networks forming sub-grain boundaries are not decorated.

Fig. 4 shows the response maps measured for a 1.2-mm thin planar detector ($\sim 0.5 \times 1$ mm^2 area) with the coherent twin boundaries crossing the crystal nearly perpendicular to its surface. The top image is a photograph of the etched CZT surface before contacting, revealing twin boundaries exiting at the surface. The image in the middle depicts the e-collection map (measured by collecting the electrons); these boundaries have a very small visible effect on the electron collection, giving the impression that they are not important. However, the h-collection map (bottom) clearly reveals charge losses associated with these twin boundaries.

Fig. 5 is another example of the (a) electron and (b) hole response maps measured for a 10×10 mm^2 area and the same 1-mm thick planar detector with sub-grain boundaries and the dislocations arranged in the walls and networks. Fig. 5(c) is the corresponding white X-ray beam diffraction-topography image; it undoubtedly illustrates why the presence of twin and sub-grain boundaries is deleterious for prospective CZT detectors.

Another example, in Fig. 6, depicts sub-grain boundaries identified by diffraction topography inside a $5 \times 5 \times 12$ mm^3 crystal, and how they affect the response of the virtual Frisch-grid detector made of this crystal to 662-keV gamma rays. The contrast in the diffraction image (a) indicates sub-grain boundaries along the long side of the crystal. The negative consequence of the presence of these defects on the device's performance is verified in the pulse-height spectrum (b) measured with 662 keV gamma-rays and the e-collection response maps (c) and (d). The response maps clearly show that a part of the detector (near the two edges) has poor charge

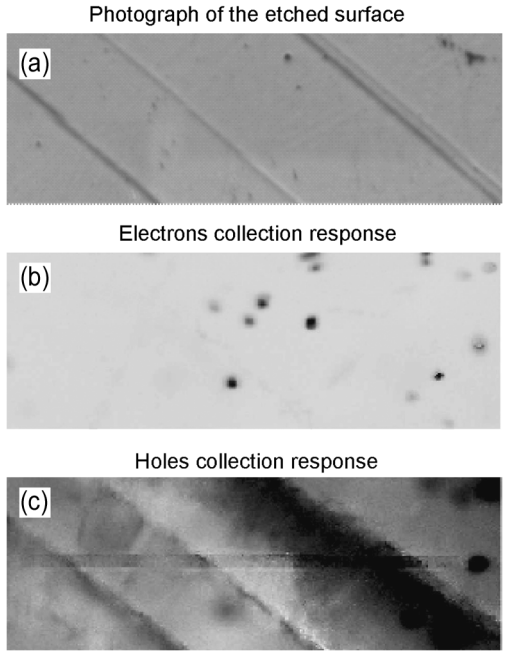

Fig. 4. Measured response maps for a 1.2-mm thin planar detector ($\sim 0.5 \times 1$ mm^2 area) with the twin boundaries. (a) a photograph of the etched CZT surface. (b) and (c) X-ray response maps measured by collecting the electrons and holes.

collection that corresponds to the large background and low peak-to-Compton ratio in the pulse-height spectrum. Due to the incomplete charge collection the full energy absorption events move from the photopeak peak area to the left side of the spectrum. The charge losses are so strong that this practically does not affect the width of the photopeak. [14] has more examples.

B. Te Inclusions

Te inclusions are responsible for the significant carrier trapping and for fluctuations in the collected charge in thick (long-drift) CZT detectors, thereby limiting their size and performance [15]–[17]. Vendors use different approaches in attempting to reduce the size and concentration of Te inclusions in their crystals below the limits at which their effects on the device's energy resolution can be corrected or even neglected.

Te inclusions that form during CZT growth [18] are 1–30 μm in diameter, typical of Te inclusions seen with IR microscopy in commercial CZT material (optical resolution is limited to 1 μm). They differ from Te precipitates that form from the nucleation of native defects. Transmission electron microscopy shows that generally they are 10–50-nm size. The concentration of Te inclusions may exceed 10^7 cm^{-3}, which is several orders-of-magnitude less than that of the Te precipitates.

Both Te precipitates and inclusions trap the charge carriers. Because of small size, precipitates behave like point defects and their collective effect is denoted only by a reduction in the total collected charge. In contrast, the charge trapped by individual inclusions can be observed directly with a highly collimated X-ray beam [5]. This signifies a difference between the charge-trapping mechanisms associated with the point-like defects and Te inclusions. In the former, the electron capture-rate is proportional to the collision frequency that is determined by

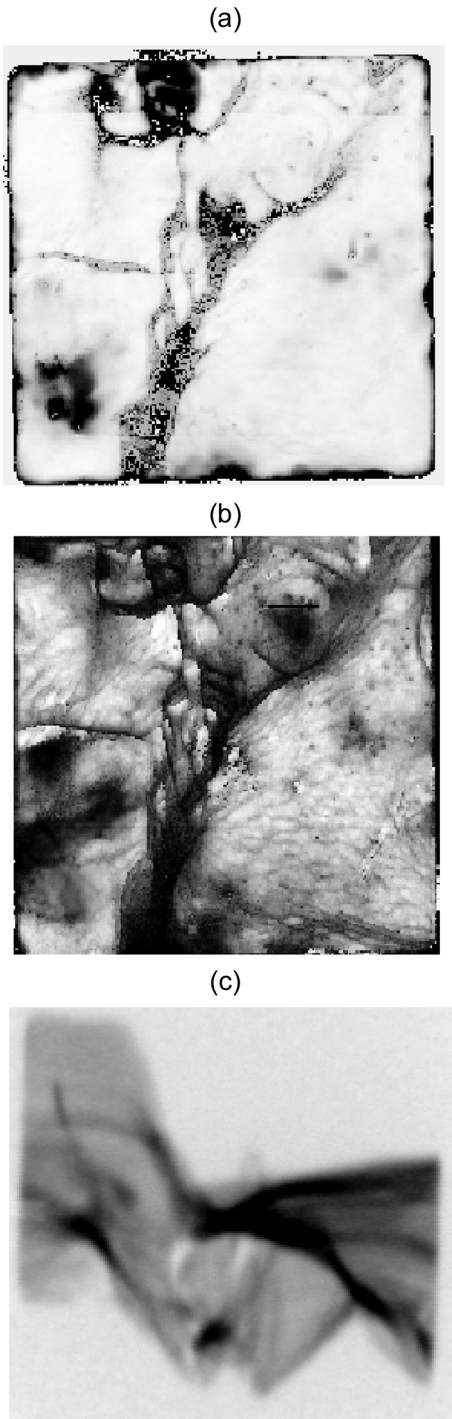

Fig. 5. (a) Electrons and (b) holes response maps measured for the 10×10 mm^2 area and a 1-mm thick planar detector with the sub-grain boundaries and the dislocations arranged in the walls and networks, also seen in an X-ray diffraction topography image (c). The step size is 25 μm, and the bias is 150 V.

the electrons' thermal velocity. Thus, the trapping process is described in terms of the electrons' lifetime, τ:

$$Q = Q_0 e^{-t/\tau}. \tag{3}$$

Because there are many collisions, the fluctuations of charge loss are negligible and enable the correction for the total charge-loss via a drift-time sensing technique.

In contrast, the electron mean-free-path, ~ 0.2 μm at room temperature, is much smaller than the typical diameter of the Te inclusions. Thus, we equate the carrier trapping with a drift-diffusion process in a discontinuous medium filled with ball-like inclusions. In the first approximation, the charge loss is proportional to the total number of inclusions that "collide" with the electron cloud, and described in terms of the attenuation length λ.

$$Q = Q_0 e^{-L/\lambda}. \tag{4}$$

Because of the few "collisions" and larger fraction of charge loss per "collision", the fluctuations in the total collected charge cannot be neglected. Modeling [16], [17] electron transport in the CZT material with Te inclusions demonstrated that the magnitude of the effect strongly depends on the ratio of the sizes of the inclusions and the electron cloud. The type of the ionization particles determines the latter. For gamma rays, simulations predicted that inclusions with diameters of less than ~ 1 μm behave as ordinary traps associated with point defects in the material. As mentioned, alpha-particles produce $\sim$10 times broader electron clouds, so then, the inclusions with diameters up to ~ 10 μm can be considered as point-like defects. In other words, alpha particles are less sensitive to fluctuations caused by Te inclusions and can only see a relatively small fraction of the Te inclusions ($\ll$1%).

Fig. 7 gives an example of a $5 \times 5 \times 12$ mm^3 virtual Frisch detector made of the crystal with Te inclusions of the size and concentrations that (a) can be considered reasonably small for a given thickness of the crystal since the energy spectrum (b) acquired remains practically unaffected. The total concentration of the inclusions measured in this sample was 4.7×10^5 cm^{-3}. Thus, this sample contains Te inclusions of small sizes and low concentration that have little or no effect on the device's performance. The energy resolution of 1.3% FWHM at 662 keV measured for this sample is attributable almost entirely to charge trapping by point defects.

The model proposed in [9], [17] considers Te inclusions as geometrical spheres that render opaque a fraction of the electrons from a cloud located within the effective diameter of the inclusion. This simplified model, depending upon a single adjustable parameter defined as the ratio of the effective- and actual-diameters of Te inclusions, described well the cumulative effects of Te inclusions on energy resolution. However, with this single parameter we were unable to reproduce precisely the "images" of the Te inclusions seen in the X-ray response maps (especially those from a wide range of the cathode biases) when the diameters and locations of Te inclusions obtained from IR microscopy measurements constituted the input data for the model. Satisfactory agreements were reached with the experiment only after individually adjusting the effective diameter for each inclusion.

These discrepancies can be explained by assuming that Te inclusions are surrounded by areas with a higher-than- average concentration of impurities-related trapping centers. Te inclusions could accumulate impurities (the gettering effect); such effects were found in other semiconductor materials grown under conditions when secondary phases are formed. Some impurities could be released back during crystal cooling. The high trapping

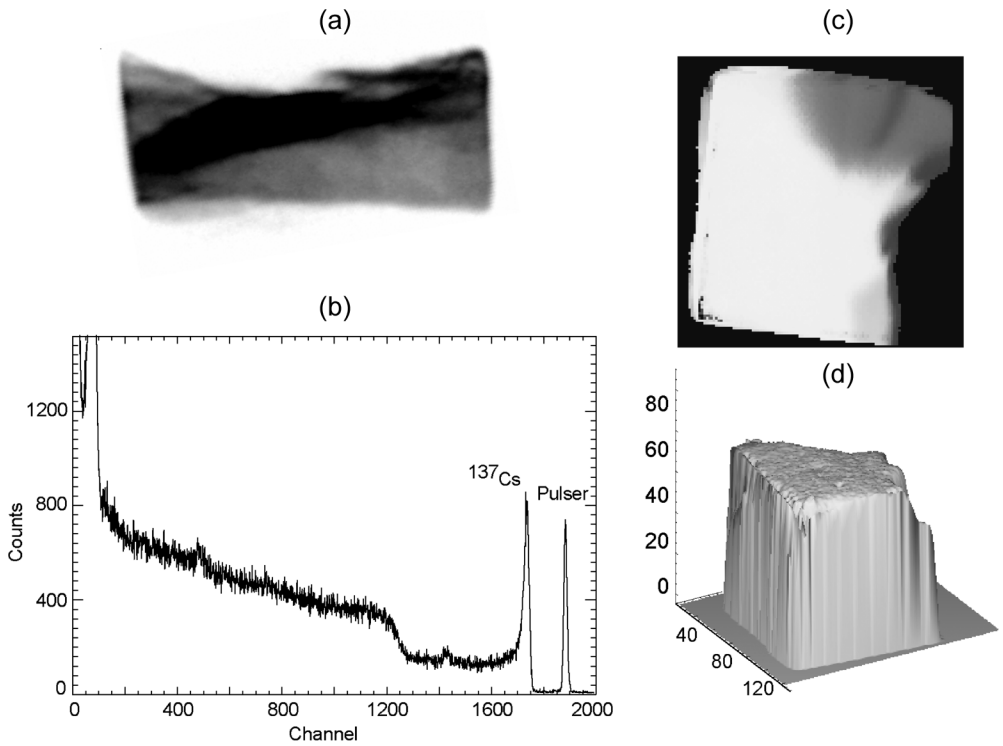

Fig. 6. Topographic image indicating a presence of sub-grain boundaries along the long side of the $5 \times 5 \times 12$ mm^3 CZT bar (a), responses measured for this detector with a ^{137}Cs source (b), and, the collimated X-ray beam (c) and (d).

areas surrounding Te inclusions change their apparent diameters, as seen in the X-ray response maps. However, generating the response maps by collecting the electrons at high biases expectedly would entail a very small additional charge loss. To enhance the electron trapping, measurements might be taken at the low cathode bias, but then electron diffusion would obscure the anticipated effect.

A presence of the trapping centers around Te inclusions is revealed by comparing the e- and h-collection maps. As discussed previously, holes are $\sim 10\times$ more sensitive to the trapping defects, while their broadening can be suppressed by taking measurements at high electric fields. Figs. 8 and 9 show the e- and h-collection response maps measured for two areas of 1.2-mm thin CZT sample. These isometric plots show the inverted response maps with the peaks representing the charge losses by Te inclusions. The inverted response maps are generated by subtracting them from the response baseline: the deeps in the response maps become the peaks. As apparent, the footprints of Te inclusions in the h-response maps are significantly larger than those in the e-response maps, suggesting that high trapping areas surround Te inclusions. We note that the diameters of Te inclusions seen in e-response maps are very close to those seen with IR microscopy. These results are in agreement with our measurements of the impurities gettering by Te inclusions [19].

C. Dislocations

It is well established that dislocations in CZT crystals are formed during thermoplastic relaxation taking place behind the melt-solid interface [20]. At high concentrations, the dislocations arrange themselves into dislocation walls that determine tilt sub-grain boundaries.

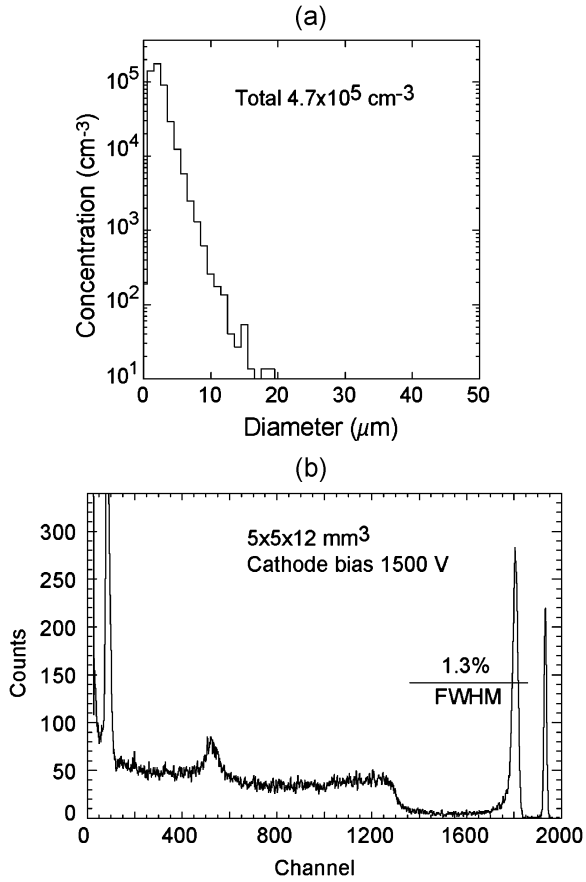

Fig. 7. Measured size distribution of inclusions for a $5 \times 5 \times 12$ mm^3 crystal (a), and the energy spectrum acquired with the same crystal configured as a virtual Frisch detector (b).

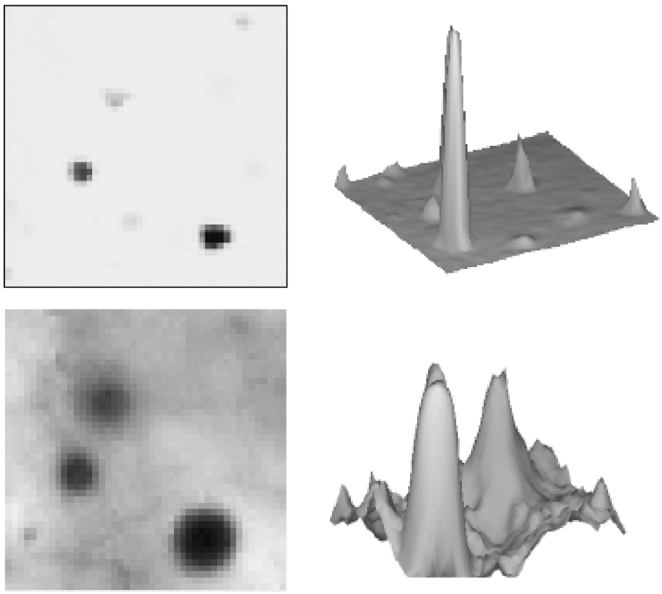

Fig. 8. X-ray response maps measured for a $0.5.5$ mm^2 area of 1.2-mm thin CZT sample by collecting the electrons (top) and holes (bottom). The cathode biases are 180- and 260- V for the electrons and holes, correspondingly. Step size is 5 μm. Isometric plots show the inverted response maps with the peaks indicating the charge losses by Te inclusions. The isometric maps are rotated by 90 degree clockwise.

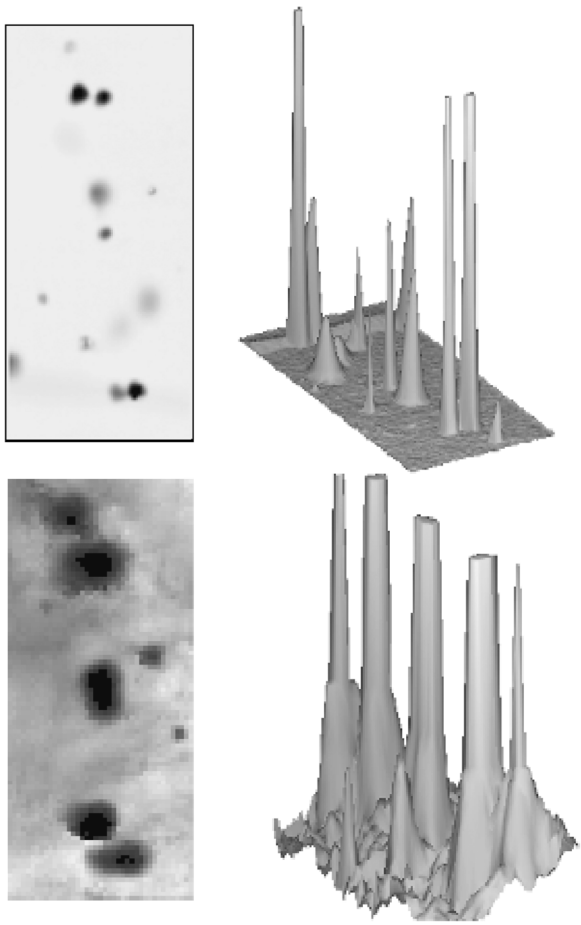

Fig. 9. Same conditions as in Fig. 8, but the sample's area is 1.5×0.5 mm^2.

Using white X-ray beam diffraction topography, we often distinguish strong internal stresses in commercial CZT crystals

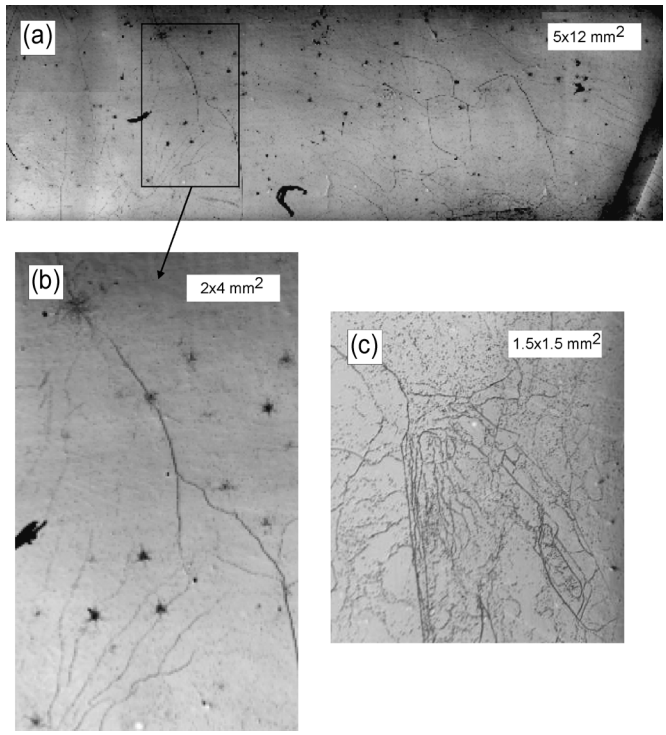

Fig. 10. Photographs of the etched surface of a commercial $5 \times 5 \times 12$ mm^3 crystal (a), (b) with clear dislocations patterns representing the dislocation walls. In some cases, the dislocations form very dense, complicated patterns (c).

[14]. Generally, the detectors fabricated from such crystals have poor spectral responses. Further, X-ray mappings of such crystals show significant non-uniformities in the charge transport, likely caused by distortions in the electric field. To verify that the crystals have high concentrations of dislocations, we employed a surface etching with a Nakagawa solution. The details of the experimental procedures and results of these studies are described elsewhere [7]. By polishing and etching the crystals several times, we traced the dislocation walls stretching deep inside the crystal's bulk. The presence of such walls that, by their nature, behave similarly to the twin and subgrain boundaries, explains why some detectors fail to perform satisfactorily. As an example, Fig. 10(a) and (b) shows the photographs of the etched surface of a commercial $5 \times 5 \times 12$ mm^3 crystal used to fabricate a virtual Frisch-grid detector [14]; the aligned etch pits represent walls of dislocations exiting at the crystal's surface. In some cases, the dislocations form very dense, complicated linear patterns, as shown in Fig. 10(c).

We measured the response maps [14] for the detectors made from crystals containing walls of dislocations to see their effect on the efficiency of charge collection. Fig. 11 shows the e-response maps measured for two representative samples (a) and (b), wherein the darker areas correspond to the areas in the device from which we obtained smaller signals. We filtered the map to enhance the faded features. The dark curved lines seen in the X-ray maps correlate with the dislocation lines in the photograph, verifying that dislocation walls affect charge transport.

Fig. 12 shows a different type of dislocation patterns that sometimes exists in commercial CZT crystals. These features, $\sim$ 500-μm diameter size, appear in low magnification images as

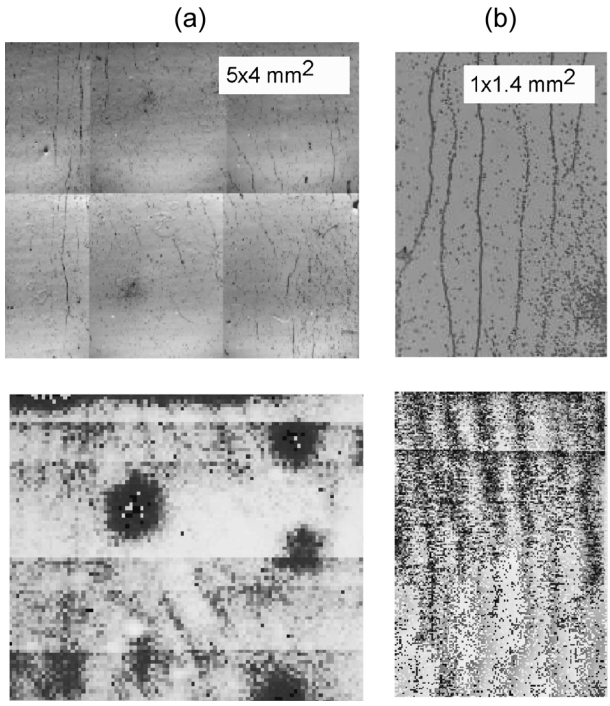

Fig. 11. Correlations between the dislocation walls seen on the etched surfaces of CZT crystals (top), and e-collection response maps (bottom) measured for two representative samples (a) and (b). Step sizes: (a) 50 μm, and (b) size 10 μm.

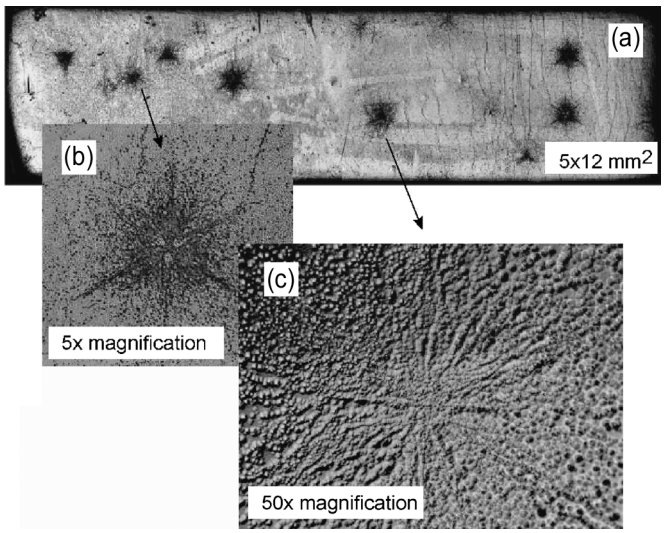

Fig. 12. Prismatic dislocations revealed by Nakagawa etching on a surface of a $5 \times 5 \times 12$ mm^3 crystal: (a) Low and (b), (c) high magnifications. These features, seen on the crystal surface as ~ 500 μm diameter star-shaped etch pits patterns, are called prismatic dislocations, whose origin in CZT crystals is unclear.

dark spots (a); they actually cause star-shaped etch-pits patterns (b), (c) called prismatic dislocations. Such dislocation patterns are generated by punching a crystal surface, but their origin in the bulk is not easy to explain. Two mechanisms were proposed as being responsible for such defects. Thus, prismatic dislocations can be caused by localized strains built up around inclusions due to their misfit with CZT bulk properties [21]. The

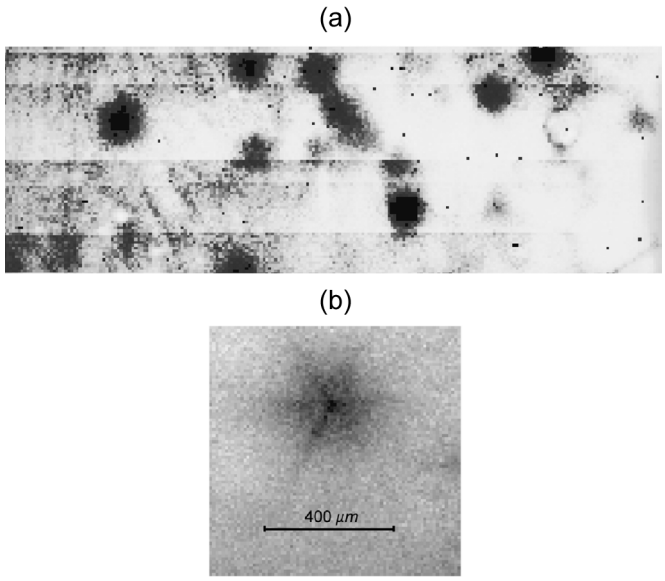

Fig. 13. The e-collection response map of a CZT sample with prismatic dislocations. A low-resolution (50 μm step) map reveals dark sports corresponding to the prismatic dislocations, while the high-resolution map (5-μm step) clearly shows the features also seen in IR photographs. The low- and high-resolution maps cover a $\sim 5 \times 10$ mm^2 (a) and $\sim 0.5 \times 0.5$ mm^2 (b) areas.

second mechanism deals with the moving dislocations, wherein their interactions with inclusions (or precipitates) generate prismatic dislocations [22]. Interestingly, no remnants of inclusions or precipitates are seen in the centers of the "stars" (b), (c).

Although the origin of the prismatic dislocations in CZT crystals is uncertain, for our purpose it is more important to illustrate their effects on charge collection in CZT detectors. We employed X-ray mapping to measure the response map of the CZT sample with prismatic defects shown in Fig. 12(a). The scan was taken over a 5×10 mm^2 area with a 50-μm resolution. The response map is shown in Fig. 13(a) wherein the dark sports correspond to the prismatic dislocations. By carrying out a 5-μm step scan [Fig. 13(b)], we resolved similar features in a single prismatic defect seen with IR microscopy.

Figs. 14 and 15 show more examples of dislocations patterns that occasionally occur in commercial CZT crystals.

D. Electric Fields Variations

We also employed high-resolution X-ray mapping to study lateral variations in the electric field of CZT detectors. Since our first measurements (reported in [23] and [24]), we tested over ten CZT detectors of different origins, geometries, and thicknesses. We confirmed our first finding that virtually all CZT detectors with thicknesses greater than $\sim$2 mm have significant lateral variations in their electric field. In some cases, the lateral shifts of the electron trajectories exceeded 1–2 mm over 10 mm drift distance in the Z-directions. The example in Fig. 16 shows the response map of a $\sim 5 \times 10$ mm^2 area of a 1-cm thick CPG device with a grounded non-collecting grid. The step size was 50 μm. The dark lines, representing the grounded strips, are not straight pointing to lateral variations in the electric field. Also, numerous small defects associated with Te inclusions appear in the map.

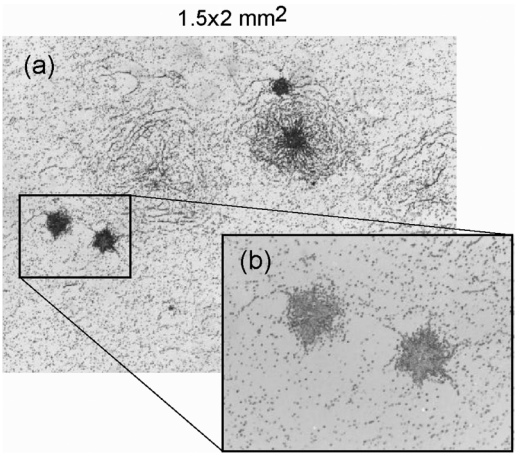

Fig. 14. Prismatic dislocations revealed on a CZT surface by Nakagawa etching: (a) Photograph of a 1.5×2 mm^2 area of a crystal surface; (b) magnified region.

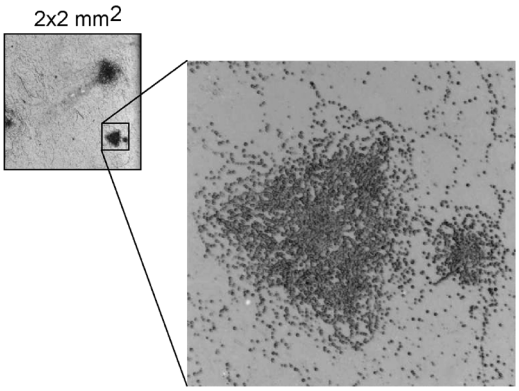

Fig. 15. Photographs of the prismatic dislocations revealed on a CZT surface: (a) 2×2 mm^2 area of a crystal surface; (b) magnified regions around a triangle-shaped pattern.

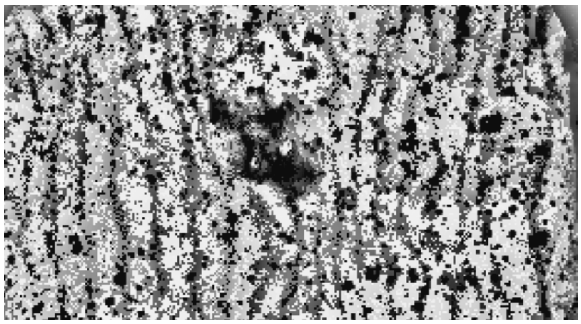

Fig. 16. The e-collection response map of a 1-cm-thick CPG device with a grounded non-collecting grid. The step size was 50 μm. Dark lines representing the grounded strips are not straight, signifying lateral variations in the electric field. The numerous small dark spots represent the Te inclusions. The area of the map is $\sim 5 \times 10$ mm^2.

The origin of such variations is unclear, but their presence correlates with the occurrence of high concentrations of dislocations and of crystal strains. The non-uniformities of the electric field make electrons travel different pathways, so causing fluctuations in the collected charge. We believe that these are the main factors affecting energy resolution in current CZT detectors.

IV. Conclusion

Using several crystal characterization techniques, we demonstrated that today's commercial CZT single crystals contain excessively high concentrations of extended defects, viz., twins, sub-grain boundaries, dislocations, and Te inclusions that affect the performance of actual CZT detectors and limit their thickness.

Many of these defects are not readily visible by eye, or under IR microscopes. Hence, vendors and detector developers often overlook them.

Extended defects are less important in thin detectors than in thick devices where they also play an important role in determining the electrical field.

References

[1] H. Chen, S. A. Awadalla, K. Iniewski, P. H. Lu, F. Harris, J. Mackenzie, T. Hasanen, W. Chen, R. Redden, G. Bindley, I. Kuvvetli, C. Budtz-Jørgensen, P. Luke, M. Amman, and J. S. Lee, "Characterization of large cadmium zinc telluride crystals grown by traveling heater method," *J. Appl. Phys.*, vol. 103, p. 014903, 2008.

[2] C. Szeles, "Advances in the crystal growth and device fabrication technology of CdZnTe room temperature radiation detectors," *IEEE Trans. Nucl. Sci.*, vol. 51, no. 3, pp. 1242–1249, 2004.

[3] Z. He and F. Zhang, "The first polaris 3-D CdZnTe detector array system," in *IEEE Nuclear Science Symp. Medical Imaging Conf.*, Honolulu, HI, Oct. 27–Nov. 3, 2007.

[4] H. F. Matare, *Defects Electronics in Semiconductor*. New York: Wiley-Interscience, 1971.

[5] G. S. Camarda, A. E. Bolotnikov, Y. Cui, A. Hossain, S. A. Awadalla, J. Mackenzie, H. Chen, and R. B. James, "Polarization studies of CdZnTe detectors using synchrotron X-ray radiation," *IEEE Trans. Nucl. Sci.*, vol. 55, no. 6, pp. 3725–3730, Dec. 2008.

[6] G. A. Carini, C. Arnone, A. E. Bolotnikov, G. S. Camarda, R. De Wames, J. H. Dinan, J. K. Markunas, B. Raghothamachar, S. Sivananthan, R. Smith, J. Zhao, Z. Zhong, and R. B. James, "Material quality characterization of CdZnTe substrates for HgCdTe epitaxy," *J. Electron. Mater.*, vol. 35, no. 6, pp. 1495–1498, 2006.

[7] A. Hossain, A. E. Bolotnikov, G. C. Camarda, Y. Cui, G. Yang, and R. B. James, "Defects in cadmium zinc telluride crystals revealed by etch pit distributions," *J. Cryst. Growth*, vol. 310, no. 21, pp. 4493–4498, 2008.

[8] A. Authier, *Dynamical Theory of X-Ray Diffraction*, revised ed. New York: Oxford Univ. Press, 2005.

[9] A. E. Bolotnikov, G. S. Camarda, G. A. Carini, Y. Cui, L. Li, and R. B. James, "Modeling the geometrical effects of Te precipitates on electron transport in CdZnTe," *Nucl. Instrum. Methods A*, vol. 571, pp. 687–698, 2007.

[10] S. A. Soldner, A. J. Narvett, D. E. Covalt, and C. Szeles, "Characterization of the charge transport uniformity of CdZnTe crystals for large-volume nuclear detector applications," *IEEE Trans. Nucl. Sci.*, vol. 51, no. 5, pp. 2443–2447, Oct. 2004.

[11] R. B. James, T. E. Schlesinger, J. C. Lund, and M. Schieber, "Cadmium zinc telluride spectrometers for gamma and X-ray applications," in *Semiconductors for Room Temperature Nuclear Detector Applications*, R. B. James and T. E. Schlesinger, Eds. New York: Academic, 1995, vol. 43, p. 334.

[12] C. Szeles and E. E. Eissler, "Current issues of high-pressure bridgman growth of semi-insulating CdZn," in *Semiconductors for Room Temperature Radiation Detector Applications II*, R. B. James, T. E. Schlesinger, P. Siffert, W. Dusi, M. R. Squillante, M. O'Connell, and M. Cuzin, Eds. Pittsburgh, PA: Materials Research Soc., 1998, vol. 487, pp. 3–12.

[13] J. R. Heffelfinger, D. L. Medlin, and R. B. James, "Analysis of grain boundaries, twin boundaries and Te inclusions in cadmium zinc telluride grown by high-pressure bridgman method," in *Semiconductors for Room Temperature Radiation Detector Applications II*, R. B. James, T. E. Schlesinger, P. Siffert, W. Dusi, M. R. Squillante, M. O'Connell, and M. Cuzin, Eds. Pittsburgh, PA: Materials Research Soc., 1998, vol. 487, p. 33.

[14] A. E. Bolotnikov, S. Babalola, G. S. Camarda, Y. Cui, S. U. Egarievwe, P. M. Fochuk, R. Hawrami, A. Hossain, J. R. James, I. J. Nakonechnyj, G. Yang, and R. B. James, "Spectral responses of virtual Frisch-grid CdZnTe detectors and their relation to IR microscopy and X-ray diffraction topography data," in *SPIE Conference on Hard X-Ray, Gamma-Ray and Neutron Detector Physics X*, R. B. James, L. A. Franks, and A. Burger, Eds., 2008, vol. 7079, pp. 707903-1–707903-16.

[15] A. E. Bolotnikov, G. S. Camarda, Y. Cui, K. T. Kohman, L. Li, M. B. Salomon, and R. B. James, "Performance-limiting defects in CdZnTe detectors," *IEEE Trans. Nucl. Sci.*, vol. 54, no. 4, pp. 821–827, Aug. 2007.

[16] A. E. Bolotnikov, N. M. Abdul-Jabber, O. S. Babalola, G. S. Camarda, Y. Cui, A. M. Hossain, E. M. Jackson, H. C. Jackson, J. A. James, K. T. Kohman, A. L. Luryi, and R. B. James, "Effects of Te inclusions on the performance of CdZnTe radiation detectors," *IEEE Trans. Nucl. Sci.*, vol. 51, no. 5, pp. 2757–2764, Oct. 2008.

[17] A. E. Bolotnikov, G. S. Camarda, G. A. Carini, Y. Cui, L. Li, and R. B. James, "Cumulative effects of Te precipitates in CdZnTe radiation detectors," *Nucl. Instrum. Methods A*, vol. 571, pp. 687–698, 2007.

[18] P. Rudolph, "Non-stoichiometry related defects at the melt growth of semiconductor compound crystals—A review," *Cryst. Res. Technol.*, vol. 38, no. 7–8, pp. 542–554, 2003.

[19] G. Yang, A. E. Bolotnikov, G. S. Camarda, Y. Cui, A. Hossain, and R. B. James, "Impurity gettering effect of Te inclusions in CdZnTe single crystals," *J. Cryst. Growth*, Oct. 2008, accepted for publication.

[20] P. Rudolph, "Dislocation cell structures in melt-grown semiconductor compound crystals," *Cryst. Res. Technol.*, vol. 40, pp. 7–20, 2005.

[21] R. D. S. Yadava, R. K. Bagai, and W. N. Borle, "Theory of Te precipitation and related effects in CdTe crystals," *J. Electron. Mater.*, vol. 21, pp. 1001–1016, 1992.

[22] T. Hatano, "Dynamics of a dislocation bypassing an impenetrable precipitate: The Hirsch mechanism revisited," *Phys. Rev. B*, vol. 74, pp. 020102-1–020102-4, 2006.

[23] A. E. Bolotnikov, G. S. Camarda, Y. Cui, A. Hossain, G. Yang, W. Yao, and R. B. James, "Internal electric-field lines distribution in CdZnTe detectors measured using an X-ray mapping technique," *IEEE Trans. Nucl. Science*, Jun. 2008, accepted for publication.

[24] G. S. Camarda, A. E. Bolotnikov, S. Babalola, Y. Cui, S. U. Egarievwe, A. Hossain, G. Yang, Z. Zhong, and R. B. James, "Effects of extended defects on the internal electric field and charge trapping in CdZnTe detectors," *IEEE Trans. Nucl. Science*, 2008, submitted for publication.